H1-prelim 07-033
March 2007

Measurement of Isolated Photon Production in Deep Inelastic Scattering at HERA

H1 Collaboration

Abstract

Results are presented on the production of isolated photons $ep \rightarrow e + \gamma + X$ in deep inelastic scattering with a four-momentum transfer squared of $4 < Q^2 < 150$ GeV^2 and a squared mass of the hadronic system $W_X^2 > 2500\,\mathrm{GeV}^2$. The cross sections, both inclusive and for events with zero or at least one additional jet, are measured with the H1 detector at the electron-proton collider HERA. The analysis is based on a total integrated luminosity of 227 pb$^-1$. The production cross section of isolated photons with a transverse energy in the range $3 < E_T^\gamma < 10$ GeV and pseudorapidity range $-1.2 < \eta^\gamma < 1.8$ is measured as a function of E_T^γ, η^γ and Q^2. The measured cross section receives contributions from photon radiation by the quark as well as wide angle bremsstrahlung of the initial and final leptons. For these processes standard Monte Carlo generators exist, PYTHIA for the radiation by the quark and RAPGAP for radiation from the lepton, as well as a full leading order calculation at parton level, which includes also quark-to-photon fragmentation. Both approaches underestimate the observed signal, particularly in the low Q^2 domain.

1 Introduction

Photons originating from the hard interaction in high energy collisions are a sensitive probe for precision tests of perturbative QCD and provide information on the proton structure. In contrast to measurements using hadrons a measurement with isolated photons minimises uncertainties from parton fragmentation, hadronisation or jet identification. Furthermore, the experimental uncertainties of the energy measurement are smaller for electromagnetic showers in the calorimeter initiated by photons than for jets of hadrons.

The measurement of isolated photons in deep-inelastic scattering (DIS) provides a test of QCD in a kinematic range with two hard scales, the four-momentum transfer squared Q^2 of the exchanged virtual photon and the transverse energy of the emitted photon. Isolated photons in DIS are produced at lowest order ($\alpha^3\alpha_s^0$), as show in figure 1. The final state photon is emitted by a quark (QQ subprocess), by wide angle radiation from the lepton (LL subprocess) or by interference (LQ subprocess). Since the photon and the scattered electron are well separated in the present analysis, low angle QED radiation is suppressed. The LL and the more interesting QQ process can not be distinguished experimentally on an event basis, but only by comparison with predictions.

Photons coupling to the interacting partons are often called “prompt” in contrast to photons from hadron decays or photons emitted by leptons. Isolated photon cross sections have been measured at various experiments and triggered theoretical discussions, e.g. [1,2]. Cross sections measured in fixed target pN experiments (see e.g. E706 [3]) show steeper decrease with the photons transverse momentum, P_T^γ, than predicted. The CDF [4] and D0 [5] experiments at the Tevatron measured the prompt photon production cross section in $p\bar{p}$ collisions. Whereas D0 finds good agreement with a NLO QCD calculation, the CDF data show again a somewhat steeper P_T^γ dependence than predicted. At HERA prompt photon cross sections have been measured by H1 and ZEUS [6–8] for photoproduction processes ($Q^2 \simeq 0$ GeV^2) and showed reasonable agreement with NLO calculations. An analysis of the inclusive isolated photon cross section in deep-inelastic scattering (DIS) with Q^2 larger than 35 GeV^2 has been published by ZEUS [9].

A thorough understanding of the standard model production mechanism of isolated photons is mandatory since isolated photons are a signature for many interesting physics processes. Many theories involving physics beyond the standard model predict final states with isolated photons produced by decays of heavy new particles.

This paper presents the measurement of isolated photon production $e + p \to e + \gamma + X$, where X is anything. Jet production in events with isolated photons and no additional jet or with at least one jet is also investigated. Isolated photons with transverse energy $3 < E_T^\gamma < 10$ GeV and pseudorapidity $-1.2 < \eta^\gamma < 1.8$ are searched for in DIS events in the kinematic regime of $4 < Q^2 < 150$ GeV^2, inelasticity $y > 0.05$ and a squared mass of the hadronic system $W_X^2 > 2500$ GeV^2. The measurement range covered by this analysis significantly extends the kinematic range probed by the previous measurement [9]. Background from high energetic neutral hadrons is largely suppressed by requiring the photon being isolated. Photon signals are identified by a multivariate analysis of the shapes of the calorimeter energy deposits, allowing their separation from neutral hadrons and their decay products. These measurements are performed using a data sample recorded by the H1 experiment at HERA in the period 1999-2005.

The results are compared to a recent leading order, $\mathcal{O}(\alpha^3\alpha_s^0)$, calculation [10,11] and to the predictions of the event generators PYTHIA [12], simulating the QQ process, and RAPGAP [13] for the LL process.

2 H1 Detector

A detailed description of the H1 detector can be found in [14]. In the following, only detector components relevant to this analysis are briefly discussed. The origin of the H1 coordinate system is the nominal ep interaction point, with the direction of the proton beam defining the positive z-axis (forward). Transverse momenta are measured in the $x-y$ plane. Polar (θ) and azimuthal (ϕ) angles are measured with respect to this reference system. The pseudo-rapidity is defined to be $\eta = -\ln\tan(\theta/2)$.

A tracking system consisting of central and forward drift chambers covering the range $7^\circ < \theta < 165^\circ$ is used to measure charged particle trajectories and to determine the position of the interaction vertex. In the central region ($25^\circ < \theta < 165^\circ$), two concentric cylindrical drift chambers (CJC) measure track trajectories in the $r-\phi$ plane and z chambers measure the z position of the track. The central tracking system provides also trigger information based on track segments in the $r-\phi$ plane and on signals in multi-wire proportional chambers. The tracking system is complemented by a silicon vertex detector ($30^\circ < \theta < 150^\circ$) and by forward drift chambers ($7^\circ < \theta < 25^\circ$). Transverse momenta ($P_T$) are determined from the curvature of the particle trajectories in a magnetic field of 1.15 T.

The liquid Argon (LAr) sampling calorimeter encloses the tracking chambers and has an asymmetric polar angle coverage of $4^\circ < \theta < 154^\circ$ and full azimuthal acceptance. It consists of an inner electromagnetic section with lead absorbers and an outer hadronic part with steel absorbers. Both sections are highly segmented in the transverse and the longitudinal direction with about $44\,000$ cells in total; the granularity increasing towards the forward direction and in the electromagnetic part. For particles coming from the ep interaction region, the laterally projected cell size in the electromagnetic part varies between 5×5 cm^2 in the forward and at most 7×13 cm^2 in the barrel region. The calorimeter is divided into eight wheels [15] along the beam axis, each of them segmented in ϕ into eight modules, separated by small regions with inactive material. The longitudinal segmentation in the different wheels varies from three (central) to four (forward) layers in the electromagnetic and from four to six in the hadronic section. The first layer has a thickness of about 3 radiation lengths. Electromagnetic shower energies are measured with a precision of $\sigma(E)/E = 12\%/\sqrt{E/\,\mathrm{GeV}} \oplus 1\%$ and hadronic energies with $\sigma(E)/E = 50\%/\sqrt{E/\,\mathrm{GeV}} \oplus 2\%$ as determined in test beam experiments [16, 17].

In the backward region $153^\circ < \theta < 178^\circ$, the energy is measured by a lead-scintillating fibre spaghetti calorimeter (SpaCal) [18]. Identification of the scattered electron in the SpaCal is improved using tracking detectors situated in front of the SpaCal, the backward drift chamber (BDC up to the year 2000) and the backward proportional chamber (BPC after 2000).

The luminosity is determined from the rate of the backward Bethe-Heitler process $ep \to ep\gamma$, measured using a photon detector located close to the beam pipe at $z = -103$ m, in the backward direction.

DIS events at Q^2 values up to 150 GeV^2 are triggered by the energy deposition of the scattered electron in the SpaCal. For particles entering the SpaCal at low radii, the SpaCal trigger is combined with a tracking requirement in the central detector [19, 20] and a signal from the central proportional chambers [21–23]. The trigger efficiency for electrons with an energy above 10 GeV varies slightly with data taking periods, but is always greater than 98%.

3 MC Generators and Corrections to the Data

Monte Carlo (MC) simulations are used to correct the data for detector acceptance and efficiency and for migration effects due to the finite resolution of the H1 detector.

The two generators PYTHIA [12] and RAPGAP [13] are used to generate photons during the hard interaction. PYTHIA [12] simulates such photons through radiation from the struck quark (QQ). Photon radiation by the electron (LL) is simulated by RAPGAP [13] (RAPGAP rad.). Both generators are based on leading order (LO) QCD matrix elements. Higher order QCD radiation is modelled using initial and final state parton showers in the leading log approximation [24]. Fragmentation into hadrons is simulated using the LUND string fragmentation model [25] as implemented in JETSET [26]. The simulation is using the CTEQ6L parton densities [27].

The combination of the signal predictions of the two MCs is not able to describe the measured cross section. The cross sections are described reasonably, if PYTHIA is scaled by a factor 2.3 and RAPGAP is not scaled. This combined "scaled signal MC" is shown in all control distributions on event level and is used to correct the data, whereas the unscaled MC prediction (signal MC) is shown in comparison to cross section measurements.

As an alternative, the HERWIG [28] generator is used to model the signal from the QQ subprocess. HERWIG simulates the fragmentation into hadrons through the decay of colourless parton clusters and uses the equivalent-photon approximation for the incoming photon beam. DIS is derived approximately as Compton scattering between the photon and a quark. This approximation is not valid for Q^2 above a few GeV^2, therefore HERWIG is only used to estimate the systematic uncertainties due to the fragmentation model dependence.

The background results from photons produced in hadronic decays in DIS events. It is modelled using the RAPGAP generator, with initial and final state radiation switched off (RAPGAP non-rad.). The background MC is reweighted to better describe non radiative DIS events with jets.

The shower shape analysis described in Section 5 requires high statistics samples of shower simulations in the whole phase space of energy and pseudorapidity. For this purpose the calorimeter signals produced by single photons and photons from decays of single neutral particles are simulated with the same detector program. These MCs are called "single particle events".

All generated events are passed through a full GEANT [29] simulation of the H1 detector and through the same reconstruction and analysis program as used for the data.

4 Event Selection

The event sample used in this analysis was collected with the H1 Detector at HERA in the period from 1999 to 2005 at a centre-of-mass energy of 318 GeV. The corresponding integrated luminosity is 227 pb^{-1}. In a first step, DIS events are identified with the scattered electron[1] in the SpaCal, in a second step an isolated photon candidate is selected. The isolation requirement largely suppresses background from photons from hadron decays.

4.1 Selection of DIS events

DIS events are selected with the scattered electron identified by a compact electromagnetic cluster [30] with an energy $E_e' > 10$ GeV and a polar angle $\theta_e < 177^\circ$ in the SpaCal. Matching signals in the backward tracking chambers are required for electron candidates with $E_e' < 18$ GeV. The scattering angle of the electron is determined from the measured impact position in the tracking chamber or the position of the energy cluster in the SpaCal and the reconstructed primary vertex.

Background from events at low Q^2 in which the electron escapes through the beam pipe and a hadron fakes the electron signature, is suppressed by the requirement that the difference between the total energy and the longitudinal momentum be in the range $35 < \Sigma(E - p_z) < 70$ GeV, where the sum includes all hadronic final state particles and the scattered electron.

Non-ep background is removed by restricting the z-coordinate of the event vertex to be within ± 40 cm of the nominal interaction vertex and requiring at least one good track in the central tracking system with polar angle $30^\circ < \theta < 150^\circ$ in addition to the track associated to the electron.

The energy E_e' and polar angle θ_e of the scattered electron candidate are used to reconstruct the inelasticity y and the four-momentum transfer squared Q^2 according to $Q_e^2 = 2\,E_e E_e'\,(1 + \cos\theta_e)$ and $y_e = 1 - E_e'/(2E_e)(1 - \cos\theta_e)$, where E_e is the electron beam energy. The analysis covers the kinematic region of $4 < Q^2 < 150$ GeV^2 and $y > 0.05$.

4.2 Selection of isolated photon candidates and jets

Photon candidates are identified as clusters in the electromagnetic section of the LAr calorimeter with a transverse energy $3 < E_T^\gamma < 10$ GeV and pseudo-rapidity $-1.2 < \eta^\gamma < 1.8$, where E_T^γ and η^γ are measured in the H1 laboratory frame. Only events with exactly one photon candidate are accepted. Less than 1% of the events are rejected because more than one photon candidate is found. To reject background from photons from hadron decays, the photon candidate is required to be isolated by the requirement that most of the transverse energy of the jet that contains the photon candidate is carried by the latter.

[1]The analysis uses data from periods when the beam lepton was either a positron or an electron. Unless explicitely stated differently, this paper uses the term electron generically to refer to both the electron and the positron.

Photon candidates are rejected if they are close to dead regions [15] of the calorimeter or if a track geometrically matches the electromagnetic cluster with a distance of closest approach to the cluster's barycentre of less than 20 cm. Neutral hadrons that decay into multiple photons, predominantly $\pi^0 \to \gamma\gamma$, constitute the main background. In most cases such decay photons lead to a common electromagnetic cluster that tends to have a wider transverse distribution than that of a single photon. Therefore a cut is applied on the transverse radius[2] of the photon candidate cluster of $R_T < 6$ cm. In addition, the invariant mass of the cluster, when combined with the closest neighbouring electromagnetic cluster having an energy above 80 MeV, must be larger than 300 MeV. This requirement rejects candidates that originate from π^0 decays with two photons reconstructed in individual clusters.

The mass of the final state hadronic system is reconstructed using the four-momenta of the incoming electron (p_e) and proton (p_p), the scattered electron (p'_e) and the photon (p_γ) as $W_X^2 = (p_e + p_p - p'_e - p_\gamma)^2$. Background from elastic Compton scattering ($p + e \to p + e + \gamma$) is suppressed by requiring that the squared invariant mass of the hadronic system be $W_X^2 > 2500$ GeV^2.

Final state hadrons are reconstructed from the deposits in the LAr calorimeter in combination with tracking information. Following the so-called "democratic" procedure [31, 32], the photon candidate and the reconstructed hadrons in each event, are combined into jets using the k_T algorithm [33], where jets are treated as massless. The algorithm is used with a P_T-weighted recombination scheme and the separation parameter R_0 is set to one. Jets are selected with a transverse momentum of $P_T^{jet} > 2.5$ GeV and a pseudorapidity in the range $-2.0 < \eta^{jet} < 2.1$. The jet containing the photon candidate is classified as photon-jet the others as hadronic jets. For hadronic jets the η^{jet}-range is restricted to $-1.0 < \eta^{jet} < 2.1$. To ensure isolation of the photon, the fraction z of the transverse energy of the photon-jet carried by the photon candidate has to be larger than 90% ($z = E_T^\gamma / E_T^{photon-jet} > 0.9$). This definition of the isolation requirement is stable against infrared divergences and thus well-suited for comparisons with perturbative QCD calculations. The distribution of the transverse energy and polar angle of the isolated photon candidates is shown in figure 2 together with the MC predictions for the scaled signal and the background. The sum of the MCs describes the data well.

Events in which none or at least one hadronic jet are found with the algorithm defined above, are called "photon plus no-jets " and "photon plus jets" respectively. The P_T^{jet} and θ^{jet} distributions for the hadronic jet with largest transverse momentum are shown in figure 3. Both distributions are reasonably well described by the sum of the scaled signal and background MCs.

In total $14\,670$ events with a scattered electron and an isolated photon candidate are selected, out of which $6\,495$ have at least one additional jet.

5 Photon Signal Extraction

The isolated photon signal is extracted using a shower shape analysis. It is based on the fact that energy depositions in the calorimeter (showers) initiated by single photons tend to be more narrow, symmetric and compact and shower later than the background. The background originates

[2]For a definition of the transverse radius see section 5.

mainly from neutral hadrons with subsequent decays to multi-photon states. The discrimination power of signal and background becomes weaker at high transverse energies, where the multi-photon clusters become more similar to a single photon cluster. Therefore events with $E_T^\gamma > 10$ GeV are excluded from the measurement.

5.1 Shower shape analysis

The extraction of the photon signal exploits the fine granularity of the electromagnetic part of the LAr calorimeter. In order to discriminate between signal photons and the background from neutral hadrons and their decay products, the calorimeter clusters corresponding to the isolated photon candidates are further analysed using six shower shape variables [34]:

1. The fraction of the energy of the electromagnetic shower contained in the cell with the largest energy deposit ("hottest" cell).

2. The fraction of the energy of the electromagnetic shower contained in four or eight (depending on the granularity of the calorimeter) contiguous cells in the first two calorimeter layers. The cells include the hottest cell and are chosen to maximise the energy which they contain ("hot core"). Both this and the first variable are sensitive to the compactness of the shower in the calorimeter.

3. The fraction of the shower's energy detected in the first calorimeter layer ("layer1"). This quantity is expected to be larger on average for multi-photon showers than for those initiated by a single photon.

4. The symmetry of a cluster is determined as the ratio of the spread (defined by root mean squared) of the transverse[3] cluster distributions along the two principal axes. A photon cluster is expected to have a symmetric cluster, whereas multi-photon clusters are more asymmetric.

5. The transverse radius of the cluster is defined by the square root of the second central transverse moment $R_T = \sqrt{\mu_2}$, where the k'th central tranverse moment of the cell distribution is given by $\mu_k = \langle[\vec{r} - \langle\vec{r}\rangle]^k\rangle$ with $\vec{r}$ being the transverse projections of the transverse cell positions and $\langle\vec{r}\rangle = (\sum_{i=0}^n E_i\vec{r_i})/\sum E_i$ the energy weighted average of the cell positions $\vec{r_i}$.

6. The kurtosis is defined by the ratio of the fourth and the squared second moment of the transverse energy distribution of the cluster cells $K = \mu_4/(\mu_2)^2 - 3$. It specifies how strongly the energy distribution is peaked; for a gaussian K equals zero.

The six shower shape variables are shown for the isolated photon candidates in figure 4. The measured distributions are compared with the sum of the background and the scaled signal MC distributions. A good agreement is observed.

[3]The transverse plane is perpendicular to the direction of the incoming particle.

5.2 Signal extraction

To discriminate between the photon and background showers, probability density functions are determined for the six shower shape variables, using simulated “single particles events” (see section 4.2) with photons and a mix (π^0, η, η', ρ, ω, $K^\star$, K_L^0, K_S^0, n and $\bar{n}$) of neutral hadrons, respectively. The relative contribution of any neutral hadron is taken from the RAPGAP MC. Though the main contribution comes from π^0 and η (roughly 90%), there is still a sizeable contribution from other neutral particles in the event sample with an isolated photon candidate.

The single particle simulation is corrected for overlap effects that can occur in a hadronic environment, which affect the cluster shapes. The cluster overlap is found to be important only in the description of the background; the signal simulation with photons is therefore not corrected. The overlap leads to a loss of photon candidates due to the distortion of the transverse cluster radius, which then exceeds in most cases the upper limit of 6 cm required in the analysis (cf. section 4.2). This loss is modelled using a probability p_{co} for cluster overlap proportional to the transverse area of the cluster $p_{co} = a \cdot R_T^2$ with $a = 0.004$ cm^2. The constant a is determined by a comparison with full event MCs in phasespace regions where sufficient statistics are available. This procedure leads to corrections of less than 10%.

The multi-dimensional photon and background probability densities are taken as the product of the respective shower shape densities. For each measured event a discriminator (D) is formed. It is defined as the photon probability density divided by the sum of the probability densities for photons and background. The discriminator produces larger values for isolated photons than for the decay photons. Figure 5 shows the discriminator distribution for the data together with the predictions of the background and the scaled signal MC. The data are nicely described by the sum of the MC predictions.

Since the shower shape densities vary significantly with E_T and η, the discriminator is determined in analysis bins in (E_T, η), with three bins in E_T and five bins in η. The bins in η correspond to different wheels of the calorimeter. The contribution of photons and neutral hadrons in any of the 15 analysis bins is determined by independent minimum-χ^2 fits of the signal (single particle photon) and background (single particle neutral hadron) discriminator distributions to the data distribution for the inclusive sample, photon plus no-jets and photon plus jets . The χ^2 function is defined to be

$$\chi^2 = \sum_i \frac{(N_{data,i} - X_{bg} N_{bg,i} - X_{sig} N_{sig,i})^2}{\sigma^2_{data,i} + X^2_{bg}\,\sigma^2_{bg,i} + X^2_{sig}\,\sigma^2_{sig,i}}$$

where i runs over the bins of the discriminator distributions. $N_{data,i}$, $N_{sig,i}$, $N_{bg,i}$ denote the i’th bin content of the data, signal and background discriminator distribution, respectively. The signal and background distributions are normalised to one. The σ_i represent the associated statistical error. X_{sig} and X_{bg}, representing the number of signal and background events, respectively, are the parameters that are determined by the fit. If the content in any histogram bin is small ($N_{data,i} < 7$), bins are merged.

The total inclusive cross section is obtained by summing the photon content of all analysis bins. The cross sections $d\sigma/dE_T^\gamma$ and $d\sigma/d\eta^\gamma$ are obtained accordingly by summing all bins

η^γ and E_T^γ, respectively. The Q^2 dependence of the cross section is determined by fitting the discriminator distribution in five different bins in Q^2. In these fits, the E_T^γ and η^γ distributions of the signal and background are assumed to follow those found in the inclusive measurement.

As a result 4372 ± 145 signal events are attributed to the inclusive data sample. In the photon plus no-jets and photon plus jets subsamples 1755 ± 106 and 2606 ± 95 signal events are found, respectively. This implies a photon yield in the selected inclusive sample described in section 4.2 of 29%. The yield is 20% for the photon plus no-jets and 39% for the photon plus jets sample, showing that the jet multiplicity for events with isolated photons is higher than for background events. The measured cross sections are compared to the unscaled MC prediction as discussed in section 3 and to LO, $\mathcal{O}(\alpha^3\alpha_s^0)$, QCD calculations [10, 11]. The cross section $\sigma(ep \to e\gamma X)$ is calculated by convoluting the parton-level lepton-quark cross sections $\hat{\sigma}(eq \to e\gamma q)$ with the parton density functions of the quarks in the proton. In the scattering amplitudes, the lepton-quark interaction is mediated by the exchange of a virtual photon with four-momentum transfer squared Q^2 and the final state photon is emitted by the lepton or the quark. The QQ contribution is dominated by the direct radiation of the photon from the quark involved in the parton level process, but contains also the contribution from quark fragmentation to a photon [35,36]. While the direct part can be calculated in perturbation theory, the fragmentation contribution has to be determined from data. It is described by a process-independent quark-to-photon fragmentation function $D_{q\to\gamma}(z)$ where z is the fraction of the quark's momentum carried by the photon. Even at leading order, the parton-level cross section contains a collinear quark-photon divergence, which is absorbed into the fragmentation function.

So far only two measurements exist, which can give direct information on the quark-to-photon fragmentation function. These were made by the LEP experiments ALEPH [32] and OPAL [37]. Only the ALEPH measurement has the precision to allow a determination of $D_{q\to\gamma}(z)$. The calculation uses the ALEPH LO parametrisation [32] of $D_{q\to\gamma}(z)$ which uses the method described in [31]. The contribution from fragmentation is not included in the MC models HERWIG and PYTHIA.

In the LL subprocess, the photon is radiated by the lepton. The reconstruction of the photon and the electron in different parts of the detector ensures that the two particles are separated, hence the LL term contains no collinear singularities. The interference term (LQ), which differs in sign for e^+p and e^-p scattering, is included in the calculation. It contributes less than 3% to the cross section.

The calculation of the isolated photon cross section is made for the same ratio of luminosities for e^+p (52.1%) and e^-p (47.9%) scattering as the data. The cuts in the theoretical calculation are adjusted to correspond to the experimental cuts described in this paper and the calculations are based on the same jet algorithm as used in this analysis. The CTEQ6L [27] leading order parametrisation of parton distributions is used. The LO predictions are compared to the data after a correction for hadronisation effects. The correction factors f_{had} are defined as the ratio of the cross sections calculated from hadrons to those from partons and are determined from the scaled signal MC. The uncertainty of the correction factor is estimated by comparing the correction factors obtained from PYTHIA with those from HERWIG. The corrections are at most 30% and the uncertainty is 5%.

6 Systematic Uncertainties

Two additional event samples are used in the determination of systematic errors. The first sample, denoted BH, consists of events with an electron reconstructed in the LAr calorimeter, a photon in the SpaCal and nothing else in the detector. Such events occur in the Bethe-Heitler process $ep \to e\gamma p$. The second (complementary) sample, denoted by DVCS, is selected by requiring an electron in the SpaCal and a photon in the LAr calorimeter. Such events originate to a large part from deeply virtual Compton scattering $ep \to e\gamma p$. The DVCS and BH selections are independent of the main selection for isolated photons and provide a clean sample of electromagnetic clusters in the LAr calorimeter. These samples are used for cluster shape studies and in-situ energy calibration.

The effect of the different systematic errors on the cross section is deduced by applying the respective variations to the MC simulation.

The systematic uncertainties considered are the following:

- Description of the shower shape variables: the measured shower shapes in the DVCS and BH event samples are compared to simulated single particle photons and electrons, respectively. The uncertainty is estimated by distorting the simulated shower shapes within limits set by DVCS and BH measurements. The fits for the signal extraction (section 5.2) are repeated with the distorted input distributions. For the single differential cross sections, systematic errors between 11% and 25% are found. The error increases with increasing E_T^γ and towards large η^γ and is independent of Q^2.
- The photon energy reconstruction is checked with the BH and DVCS events. For the BH events the cluster transverse energy is compared with the transverse momentum of the track. For DVCS events the energy of the cluster is compared to the energy calculated using the double angle method [38]. The photon energy scale uncertainty estimated with this method varies from 1% for photons detected in the backward region to 4% for forward photons. The resulting error on the total inclusive cross section is $+3.6\%$ and -2.6%.
- Photon angle: an uncertainty of 3 mrad (4 mrad for $\eta_\gamma > 1.4$) is applied to the measurement of the angle of the photon. This uncertainty is found by comparing the angular measurements of the track and the cluster for BH electrons. It gives rise to an error on the total inclusive cross section of $+0.1$ and -0.7%.
- Electron: an uncertainty of $1 - 2\%$ is applied to the energy of the scattered electron and an uncertainty of 2 mrad to the measurement of the scattering angle. The resulting error on the total inclusive cross section is $+1.9\%$ and -2.9%.
- Hadronic final state: a 3% uncertainty is applied to the energy of hadronic final state objects [39], it affects the measured cross section by $+1.2\%$ and -0.7%.
- A 5% uncertainty is applied on the normalisation of the correction of the cluster overlap.
- The model dependence of the corrections is studied by comparing PYTHIA and HERWIG simulations. A value of value of 5% is found for the inclusive and the photon plus jets and 10% for the photon plus no-jets cross sections.

- The uncertainty of the ratio of the PYTHIA and RAPGAP contributions is taken into account by varying the scaling factor for PYTHIA from 1.5 to 3. For the double differential cross section, a maximum systematic error of 5% is found. In regions with $\eta^{\gamma} > -0.6$, the systematic error is below 1%.

- There is only a small dependence on the choice of the parton density function which is neglected.

- A 1% uncertainty in the description of the trigger efficiency by the MCs is included in the systematic error.

- The tracking inefficiency in the data was found to be 1% resulting in an uncertainty on the rejection of charged particles. The systematic uncertainty on the requirement of a central track in the detector is found to be below 1%. The uncertainty in the track efficiency results in an error of $\pm 0.3\%$ for the total inclusive cross section.

- The uncertainty in the probability for conversion of the photons before entering the calorimeter is estimated to be 2%.

- The uncertainty on the luminosity measurement is 2%.

The individual effects of these experimental uncertainties are combined in each bin in quadrature. The systematic uncertainty obtained on the total inclusive cross section is $+13.6\%$ and -15.5%. The largest contribution to this uncertainty arises from the systematic effect attributed to the description of the shower shapes.

7 Results

The cross section is measured in the phase space defined in table 1. In each bin of the kinematic variables, the cross section is computed from the number of events with photons in the bin, fully corrected for acceptance and smearing effects using the scaled signal MC. The differential cross sections are compared with the MC predictions from the unscaled PYTHIA plus RAPGAP (signal MC) and the LO calculation.

7.1 Inclusive isolated photon cross sections

The measured inclusive isolated photon cross section amounts to

$$\sigma(ep \to e\gamma X) = 50.3 \pm 1.7\ (\text{stat})\ {}^{+6.8}_{-7.8}\ (\text{syst})\ \text{pb}.$$

The LO calculation predicts a cross section of 28.2 pb, while the signal MC expectation is 26.4 pb. Both predictions significantly underestimate the total inclusive cross section, by 43% for the LO and 47% for the signal MC prediction.

Differential cross sections $d\sigma/dE_T^{\gamma}$, $d\sigma/d\eta^{\gamma}$ and $d\sigma/dQ^2$ are presented in table 2 and in figure 6 together with the predictions by the signal MC and the LO calculation. The correction factor f_{had} for the correction of the LO calculation to hadron level is listed in all the cross section tables. The uncertainty of the hadron corrections amounts to 5%.

The LO calculation lies furthest below the data at low Q^2. It describes reasonably the shapes of the data distributions in E_T^γ and η^γ, with some tendency to lie further below the data at high transverse energies and low and medium rapidities of the photon. The LL and QQ contributions are shown separately in figure 6. Their relative contribution depends strongly on η^γ and Q^2. At low η^γ, close to the scattered electron, the LL contribution is of similar magnitude as that of QQ. At high and medium η^γ, radiation by the quark dominates. The LQ contribution is included in the sum, but not shown separately as it amounts to a few percent of the total cross section only.

The cross section predicted by the signal MC agrees reasonably well with the LO calculation. The PYTHIA prediction follows the shape of the QQ contribution, whereas the RAPGAP prediction for the photons radiated from the electron follow the LL contribution. The sum of the two MC predictions underestimates the data most significantly in the region of low Q^2, high E_T^γ and low and medium η^γ, similar to the LO calculation. Different parton density functions for the proton may change the signal MC prediction by up to 5%. As the LO calculation and the signal MC prediction give very similar results, further cross sections are only shown in comparison to the LO calculation.

Figure 7 and table 3 present the E_T^γ dependence of the cross section in five different bins in η^γ, corresponding to the wheel structure of the calorimeter. At low η^γ, the LL and the QQ term are of similar magnitude. As the LL term is very small for $\eta^\gamma > -0.6$, the underestimation of the data by the calculation and the signal MC of roughly 45% can be attributed mainly to an underestimated QQ contribution; the shape of the distributions is reasonably reproduced.

At $Q^2 > 40\,\mathrm{GeV}^2$, the agreement of the predictions with the data is somewhat better, as can be seen in figure 8 and table 4. The total inclusive cross section for $Q^2 > 40$ GeV^2 is

$$\sigma(ep \rightarrow e\gamma X) = 14.0 \pm 0.8\ (\mathrm{stat})\ ^{+2.1}_{-2.1}\ (\mathrm{syst})\ \mathrm{pb}.$$

The LO (10.3 pb) and the signal MC (8.8 pb) predictions still lie below the data but only by roughly 30%, and the shapes of the $d\sigma/dE_T^\gamma$ and $d\sigma/d\eta^\gamma$ distributions are well reproduced. With the higher cut on Q^2, the relative contribution of final state radiation by the electron is higher than at low Q^2.

The ZEUS collaboration previously measured an inclusive isolated photon cross section of $5.64 \pm 0.58(\mathrm{stat})\ ^{+0.47}_{-0.72}$ (syst) pb [9] for $Q^2 > 35\,\mathrm{GeV}^2$, $5 < E_T^\gamma < 10\,\mathrm{GeV}$ and $-0.7 < \eta^\gamma < 0.9$. It was described reasonably well by the same LO ($\alpha^3\alpha_s^0$) calculation as used for comparison in this analysis [10]. It should be noted that for this comparison the LO calculation was not corrected for hadronisation effects which decrease the prediction at central rapidities by roughly 20% (cf. table 4). Our measurement significantly extends the kinematical region probed by ZEUS in transverse energy, pseudorapidity and Q^2. If restricted to the same phasespace, it agrees with the ZEUS result.

7.2 Photon plus no-jets and Photon plus jets cross sections

The cross section for jet production in association with isolated photons is studied, using events with no or at least one hadronic jet. The measurement is performed in the phase space defined for the inclusive cross section with an additional jet requirement or veto as shown in table 1.

In the photon plus no-jets sample there is little hadronic activity in the final state besides that contained in the photon-jet and the proton remnant. The quark-to-photon fragmentation enters already at lowest order ($\alpha^3\alpha_s^0$) [11], in contrast to the photon plus jets sample where the fragmentation contribution is of the order $\alpha^3\alpha_s^1$, giving the photon plus no-jets sample particular interest.

The total cross section for photon plus no-jets is measured as

$$\sigma(ep \to e\gamma Y) = 18.7 \pm 1.2 \text{ (stat) } {}^{+3.3}_{-3.4} \text{ (syst) pb},$$

where Y contains no hadronic jet in the acceptance of the measurement. The cross section for the photon plus jets is

$$\sigma(ep \to e\gamma jetX) = 31.6 \pm 1.2 \text{ (stat) } {}^{+4.2}_{-4.8}\text{(syst) pb}.$$

The prediction of the LO calculation is $11.7(16.7)$ pb and from signal MC $10.0(16.4)$ pb for the photon plus no-jets (photon plus jets), respectively. Both predictions are significantly lower than the data, the scaling factors being very similar to the factors for the inclusive measurement.

Figure 9 and table 5 show the differential cross sections $d\sigma/dE_T^\gamma$ (a, b), $d\sigma/d\eta^\gamma$ (c, d) and $d\sigma/dQ^2$ (e, f) for the photon plus no-jets (jets) selection in comparison with the LO predictions. The $d\sigma/dE_T^\gamma$ and $d\sigma/d\eta^\gamma$ distributions are described reasonably well in shape. For both samples the predictions are furthest below the data at low Q^2, where the QQ term dominates. The LL contribution is largely suppressed for the photon plus no-jets sample due to the cut on W_X^2. Since the fragmentation contribution to the cross section enters the two samples at different orders, the observed excess can not solely be attributed to an underestimation of that contribution. The cross section for photon plus jets production is roughly two times higher than for photon plus no-jets . This is in contrast to the inclusive $ep \to eX$ cross section, where topologies with an additional jet are suppressed by $\mathcal{O}(\alpha_s)$. The above observation reflects the fact that both cross sections have the same order in perturbative QCD.

8 Conclusions

The cross section for isolated photon production in deep inelastic scattering has been measured in the squared momentum transfer range $4 < Q^2 < 150$ GeV^2. A LO calculation, and alternatively the PYTHIA generator for the simulation of photons radiated by the quark (QQ) together with photons radiated from the electron (LL) as predicted by RAPGAP describe the shape of the E_T^γ and η^γ distributions reasonably well, but lie below the data by roughly 40% (LO) and 50% (MC). Both, the LO calculation and the MC predictions are most significantly below the data at low Q^2. The two LO processes contributing to the cross section, radiation by the quark and emission from the electron, differ significantly in their η^γ distribution. At low η^γ, the LL and QQ contributions are of similar magnitude. At medium and high η^γ, the radiation by the quark is dominant. The cross sections in different bins in η^γ show that, for $\eta^\gamma > -0.6$, where the LL contribution is small, the difference can mainly be attributed to an underestimation of the QQ contribution.

The cross sections for events with no or at least one hadronic jet are underestimated by the LO and MC predictions by a similar factor as in the inclusive measurement. Again the expectations are furthest below the data at low Q^2. The shapes of $d\sigma/dE_T^\gamma$ and $d\sigma/d\eta^\gamma$ are described reasonably well. The total photon plus jets cross section is roughly double the photon plus no-jets cross section as expected from the calculations.

The present measurements indicate the need for higher order corrections in the calculation of isolated photon phenomena in deep-inelastic ep scattering.

Acknowledgements

We are grateful to the HERA machine group whose outstanding efforts have made this experiment possible. We thank the engineers and technicians for their work in constructing and maintaining the H1 detector, our funding agencies for financial support, the DESY technical staff for continual assistance and the DESY directorate for support and for the hospitality which they extend to the non DESY members of the collaboration. We would like to thank Aude Gehrmann-De Ridder, Thomas Gehrmann and Eva Poulsen for providing the LO calculations and many helpful discussions.

References

[1] P. Aurenche, M. Fontannaz, J. P. Guillet, E. Pilon and M. Werlen, Phys. Rev. D **73** (2006) 094007 [arXiv:hep-ph/0602133].

[2] J. Gayler, Acta Phys. Polon. B **37** (2006) 715 [arXiv:hep-ex/0511035].

[3] L. Apanasevich *et al.* [Fermilab E706 Collaboration], "Measurement of direct photon production at Tevatron fixed target energies," Phys. Rev. D **70** (2004) 092009 [arXiv:hep-ex/0407011].

[4] F. Abe *et al.* [CDF Collaboration], "A Precision measurement of the prompt photon cross-section in $p\bar{p}$ collisions at $\sqrt{s} = 1.8$ TeV," Phys. Rev. Lett. **73** (1994) 2662 [Erratum-ibid. **74** (1995) 1891].
D. Acosta *et al.* [CDF Collaboration], "Comparison of the isolated direct photon cross sections in $p\bar{p}$ collisions at $\sqrt{s} = 1.8$-TeV and $\sqrt{s} = 0.63$-TeV," Phys. Rev. D **65** (2002) 112003 [arXiv:hep-ex/0201004].
D. Acosta *et al.* [CDF Collaboration], "Direct photon cross section with conversions at CDF," Phys. Rev. D **70** (2004) 074008 [arXiv:hep-ex/0404022].

D. Acosta *et al.* [CDF Collaboration], "Measurement of the cross section for prompt diphoton production in $p\bar{p}$ collisions at $\sqrt{s} = 1.96$ TeV," Phys. Rev. Lett. **95** (2005) 022003 [arXiv:hep-ex/0412050].

[5] B. Abbott *et al.* [D0 Collaboration], "The isolated photon cross-section in $p\bar{p}$ collisions at $\sqrt{s} = 1.8$ TeV," Phys. Rev. Lett. **84** (2000) 2786 [arXiv:hep-ex/9912017].
V. M. Abazov *et al.* [D0 Collaboration], "Measurement of the isolated photon cross section in $p\bar{p}$ collisions at $\sqrt{s}$ = 1.96-TeV," Phys. Lett. B **639** (2006) 151 [arXiv:hep-ex/0511054].

[6] J. Breitweg *et al.* [ZEUS Collaboration], "Measurement of inclusive prompt photon photoproduction at HERA," Phys. Lett. B **472** (2000) 175 [arXiv:hep-ex/9910045].

[7] A. Aktas *et al.* [H1 Collaboration], "Measurement of prompt photon cross sections in photoproduction at HERA," Eur. Phys. J. C **38** (2005) 437 [arXiv:hep-ex/0407018].

[8] S. Chekanov *et al.* [ZEUS Collaboration], Eur. Phys. J. C **49** (2007) 511 [arXiv:hep-ex/0608028].

[9] S. Chekanov *et al.* [ZEUS Collaboration], "Observation of isolated high-E(T) photons in deep inelastic scattering," Phys. Lett. B **595** (2004) 86 [arXiv:hep-ex/0402019].

[10] A. Gehrmann-De Ridder, T. Gehrmann and E. Poulsen, "Isolated photons in deep inelastic scattering," Phys. Rev. Lett. **96** (2006) 132002 [arXiv:hep-ph/0601073].

[11] A. Gehrmann-De Ridder, T. Gehrmann and E. Poulsen, "Measuring the photon fragmentation function at HERA," Eur. Phys. J. C **47** (2006) 395 [arXiv:hep-ph/0604030].

[12] T. Sjöstrand *et al.*, PYTHIA 6.2 Physics and Manual (Version 6.224 is used) [hep-ph/0108264].

[13] H. Jung, Comput. Phys. Commun. **86** (1995) 147 (Version 3.1 is used).
(see also http://www.desy.de/ jung/rapgap.html).

[14] "The H1-Detector at HERA" I. Abt *et al.*, Nucl. Instr. and Meth. **A 386** (1997) 310, ibid, 348.

[15] B. Andrieu *et al.* [H1 Calorimeter Group], "The H1 liquid argon calorimeter system," Nucl. Instrum. Meth. A **336** (1993) 460.

[16] B. Andrieu *et al.* [H1 Calorimeter Group], "Beam tests and calibration of the H1 liquid argon calorimeter with electrons," Nucl. Instrum. Meth. A **350** (1994) 57.

[17] B. Andrieu *et al.* [H1 Calorimeter Group], "Results from pion calibration runs for the H1 liquid argon calorimeter and comparisons with simulations,"Nucl. Instrum. Meth. A **336** (1993) 499.

[18] R. D. Appuhn *et al.*, "The H1 lead/scintillating-fibre calorimeter," Nucl. Instrum. Meth. A **386** (1997) 397.

[19] T. Wolff *et al.*, "A driftchamber track finder for the first level trigger of the H1 experiment," Nucl. Instrum. Meth. A **323** (1992) 537.

[20] A. Baird *et al.*, Nucl. Instrum. Meth. A **461** (2001) 461,
A. Schöning *et al.*, Nucl. Instrum. Meth. A **518** (2004) 542.

[21] K. Muller *et al.*, "Construction and performance of a thin cylindrical multiwire proportional chamber with cathode pad readout for the H1 experiment," Nucl. Instrum. Meth. A **312**, 457 (1992).

[22] S. Eichenberger *et al.*, "A fast pipelined trigger for the H1 experiment based on multiwire proportional chamber signals," Nucl. Instrum. Meth. A **323**, 532 (1992).

[23] J. Becker *et al.*, "A vertex trigger based on cylindrical multiwire proportional chambers," arXiv:physics/0701002.

[24] M. Bengtsson and T. Sjostrand, "Parton Showers In Leptoproduction Events," Z. Phys. C **37** (1988) 465.

[25] B. Andersson, G. Gustafson, G. Ingelman and T. Sjöstrand, "Parton Fragmentation And String Dynamics," Phys. Rept. **97** (1983) 31.

[26] T. Sjöstrand, Comput. Phys. Commun.**82** (1994) 74.

[27] D. Stump, J. Huston, J. Pumplin, W. K. Tung, H. L. Lai, S. Kuhlmann and J. F. Owens, "Inclusive jet production, parton distributions, and the search for new physics," JHEP **0310** (2003) 046 [arXiv:hep-ph/0303013].

[28] G. Corcella *et al.*, HERWIG 6.5 Release Note **135** (2001) 128, [hep-ph/0210213] (Version 6.505 is used).

[29] GEANT 3, R. Brun *et al.*, CERN_DD/EE/84-1.

[30] C. Adloff *et al.* [H1 Collaboration], "Deep-inelastic inclusive e p scattering at low x and a determination of alpha(s)," Eur. Phys. J. C **21** (2001) 33 [arXiv:hep-ex/0012053].

[31] E. W. N. Glover and A. G. Morgan, "Measuring the photon fragmentation function at LEP," Z. Phys. C **62** (1994) 311.

[32] D. Buskulic *et al.* [ALEPH Collaboration], "First measurement of the quark to photon fragmentation function," Z. Phys. C **69** (1996) 365.

[33] S. D. Ellis and D. E. Soper, "Successive combination jet algorithm for hadron collisions," Phys. Rev. D **48** (1993) 3160 [arXiv:hep-ph/9305266].

[34] C. Schmitz, Ph.D. Thesis Zürich University, 2007, in preparation, available at http://www-h1.desy.de/publications/theses_list.html.

[35] K. Koller, H. G. Sander, T. F. Walsh and P. M. Zerwas, "Angular Asymmetries Of E+ E- Annihilation To Three Jets," Z. Phys. C **6**, 131 (1980).

[36] M. Gluck, L. E. Gordon, E. Reya and W. Vogelsang, "High P(T) photon production at p anti-p collider," Phys. Rev. Lett. **73** (1994) 388.

[37] K. Ackerstaff *et al.* [OPAL Collaboration], "Measurement of the quark to photon fragmentation function through the inclusive production of prompt photons in hadronic Z0 decays," Eur. Phys. J. C **2** (1998) 39 [arXiv:hep-ex/9708020].

[38] S. Bentvelsen *et al.* , Proceedings of the Workshop "Physics at HERA", vol.1, eds. W. Buchmüller, G. Ingelman, DESY (1992) 23;
C. Hoeger, ibid.,43.

[39] C. Adloff *et al.* [H1 Collaboration], "Measurement of neutral and charged current cross-sections in positron proton collisions at large momentum transfer," Eur. Phys. J. C **13** (2000) 609 [arXiv:hep-ex/9908059].

Isolated photon cross section phase space	
Inclusive cross section	$3 < E_T^\gamma < 10$ GeV $-1.2 < \eta^\gamma < 1.8$ $z = E_T^\gamma / E_T^{photon-jet} > 0.9$ $E_e' > 10$ GeV $153 < \theta_e < 177°$ $4 < Q^2 < 150$ GeV^2 $W_X^2 > 2500$ GeV^2 $y > 0.05$ $\sqrt{s} = 319$ GeV
Jet definition	k_T algorithm with P_T-weighted recombination scheme [33], $R_0 = 1$ $P_T^{jet} > 2.5$ GeV $-1.0 < \eta^{jet} < 2.1$
E_T and η are measured in the H1 laboratory frame	

Table 1: The phase space regions in which isolated prompt photon cross sections are measured and definition the kinematic region for jets.

H1 Inclusive Isolated Photon Cross Sections					
E_T^γ [GeV]		$d\sigma/dE_T^\gamma$ [pb/GeV]	stat.	syst.	f_{had}
3.0	4.0	16.98	± 1.20	$^{+2.79}_{-2.61}$	0.78
4.0	6.0	10.51	± 0.47	$^{+1.50}_{-1.86}$	0.89
6.0	10.0	3.08	± 0.20	$^{+0.46}_{-0.60}$	0.98
η^γ		$d\sigma/d\eta^\gamma$ [pb]	stat.	syst.	f_{had}
-1.2	-0.6	26.15	± 1.67	$^{+3.60}_{-4.16}$	0.92
-0.6	0.2	20.69	± 1.34	$^{+3.53}_{-3.73}$	0.85
0.2	0.9	15.83	± 0.93	$^{+1.97}_{-3.25}$	0.81
0.9	1.4	9.57	± 0.87	$^{+1.99}_{-2.00}$	0.80
1.4	1.8	5.50	± 1.15	$^{+1.04}_{-1.75}$	0.80
Q^2 [GeV^2]		$d\sigma/dQ^2$ [pb/GeV^2]	stat.	syst.	f_{had}
4.0	10.0	2.48	± 0.21	$^{+0.34}_{-0.41}$	0.87
10.0	20.0	1.17	± 0.07	$^{+0.19}_{-0.21}$	0.83
20.0	40.0	0.52	± 0.03	$^{+0.07}_{-0.10}$	0.81
40.0	80.0	0.235	± 0.013	$^{+0.033}_{-0.048}$	0.83
80.0	150.	0.063	± 0.006	$^{+0.009}_{-0.012}$	0.87

Table 2: Inclusive differential isolated photon cross sections in the kinematic range specified in table 1. f_{had} denotes the hadronisation correction factor applied to the LO calculation.

H1 Inclusive Isolated Photon Cross Sections					
E_T^γ [GeV]		$d\sigma/dE_T^\gamma$ [pb/GeV]	stat.	syst.	f_{had}
$-1.2 < \eta^\gamma < -0.6$					
3.0	4.0	4.86	± 0.67	$^{+0.88}_{-0.63}$	0.86
4.0	6.0	3.46	± 0.28	$^{+0.48}_{-0.66}$	0.96
6.0	10.0	0.98	± 0.12	$^{+0.13}_{-0.23}$	1.00
$-0.6 < \eta^\gamma < 0.2$					
3.0	4.0	5.81	± 0.75	$^{+1.27}_{-1.20}$	0.76
4.0	6.0	3.20	± 0.28	$^{+0.56}_{-0.64}$	0.88
6.0	10.0	1.09	± 0.13	$^{+0.15}_{-0.16}$	0.99
$0.2 < \eta^\gamma < 0.9$					
3.0	4.0	3.94	± 0.51	$^{+0.59}_{-0.72}$	0.72
4.0	6.0	2.39	± 0.16	$^{+0.28}_{-0.51}$	0.84
6.0	10.0	0.59	± 0.06	$^{+0.09}_{-0.14}$	0.96
$0.9 < \eta^\gamma < 1.4$					
3.0	4.0	1.66	± 0.31	$^{+0.22}_{-0.31}$	0.69
4.0	6.0	0.82	± 0.12	$^{+0.21}_{-0.16}$	0.82
6.0	10.0	0.37	± 0.05	$^{+0.10}_{-0.09}$	0.96
$1.4 < \eta^\gamma < 1.8$					
3.0	4.0	0.72	± 0.28	$^{+0.23}_{-0.21}$	0.70
4.0	6.0	0.64	± 0.16	$^{+0.09}_{-0.22}$	0.81
6.0	10.0	0.049	± 0.045	$^{+0.009}_{-0.016}$	0.94

Table 3: Inclusive differential isolated photon cross sections $d\sigma/dE_T^\gamma$ for $4 < Q^2 < 150$ GeV^2 for different η^γ-bins that correspond to the wheel structure of the LAr calorimeter (see text). The kinematic region is defined in table 1. f_{had} denotes the hadronisation correction factor applied to the LO calculation.

H1 Inclusive Isolated Photon Cross Sections for $Q^2 > 40$ GeV^2					
E_T^γ [GeV]		$d\sigma/dE_T^\gamma$ [pb/GeV]	stat.	syst.	f_{had}
3.0	4.0	3.70	± 0.39	$^{+0.63}_{-0.58}$	0.80
4.0	6.0	2.53	± 0.23	$^{+0.43}_{-0.43}$	0.87
6.0	10.0	1.30	± 0.15	$^{+0.19}_{-0.27}$	0.96
η^γ		$d\sigma/d\eta^\gamma$ [pb]	stat.	syst.	f_{had}
-1.2	-0.6	9.61	± 1.00	$^{+1.48}_{-2.02}$	0.97
-0.6	0.2	5.13	± 0.59	$^{+0.92}_{-0.97}$	0.86
0.2	0.9	3.49	± 0.32	$^{+0.45}_{-0.72}$	0.78
0.9	1.4	2.37	± 0.33	$^{+0.49}_{-0.47}$	0.76
1.4	1.8	1.12	± 0.51	$^{+0.21}_{-0.34}$	0.73

Table 4: Inclusive differential isolated photon cross sections in the kinematic range specified in table 1 and $40 < Q^2 < 150$ GeV^2. f_{had} denotes the hadronisation correction factor applied to the LO calculation.

H1 Photon plus no-Jets (Jets) Cross Sections									
		Photon plus no-jets				**Photon plus jets**			
E_T^γ [GeV]		$d\sigma/dE_T^\gamma$ [pb/GeV]	stat.	syst.	f_{had}	$d\sigma/dE_T^\gamma$ [pb/GeV]	stat.	syst.	f_{had}
3.0	4.0	8.10	± 0.93	$^{+1.82}_{-1.48}$	0.75	8.85	± 0.70	$^{+1.37}_{-1.38}$	0.82
4.0	6.0	3.79	± 0.29	$^{+0.69}_{-0.77}$	0.91	6.65	± 0.35	$^{+0.92}_{-1.15}$	0.89
6.0	10.0	0.77	± 0.10	$^{+0.14}_{-0.18}$	1.10	2.35	± 0.17	$^{+0.35}_{-0.46}$	0.97
η^γ		$d\sigma/d\eta^\gamma$ [pb]	stat.	syst.	f_{had}	$d\sigma/d\eta^\gamma$ [pb]	stat.	syst.	f_{had}
-1.2	-0.6	9.30	± 1.07	$^{+1.53}_{-1.72}$	0.88	16.61	± 1.20	$^{+2.67}_{-2.64}$	0.97
-0.6	0.2	8.46	± 0.95	$^{+1.73}_{-1.84}$	0.81	12.32	± 0.90	$^{+2.15}_{-2.19}$	0.88
0.2	0.9	5.98	± 0.71	$^{+1.16}_{-1.34}$	0.82	9.94	± 0.59	$^{+1.16}_{-2.03}$	0.81
0.9	1.4	2.57	± 0.47	$^{+0.64}_{-0.61}$	0.85	6.99	± 0.73	$^{+1.38}_{-1.40}$	0.79
1.4	1.8	2.40	± 0.73	$^{+0.78}_{-0.74}$	0.97	3.22	± 0.85	$^{+0.61}_{-1.01}$	0.71
Q^2 [GeV^2]		$d\sigma/dQ^2$ [pb/GeV^2]	stat.	syst.	f_{had}	$d\sigma/dQ^2$ [pb/GeV^2]	stat.	syst.	f_{had}
4.0	10.0	1.09	± 0.16	$^{+0.21}_{-0.22}$	0.96	1.39	± 0.13	$^{+0.20}_{-0.22}$	0.85
10.0	20.0	0.44	± 0.05	$^{+0.09}_{-0.09}$	0.88	0.76	± 0.05	$^{+0.11}_{-0.14}$	0.85
20.0	40.0	0.21	± 0.02	$^{+0.04}_{-0.05}$	0.93	0.31	± 0.02	$^{+0.04}_{-0.06}$	0.82
40.0	80.0	0.071	± 0.008	$^{+0.012}_{-0.017}$	1.09	0.162	± 0.010	$^{+0.024}_{-0.033}$	0.86
80.0	150.	0.021	± 0.004	$^{+0.005}_{-0.007}$	1.35	0.040	± 0.005	$^{+0.005}_{-0.007}$	0.73

Table 5: Differential isolated photon cross sections in the kinematic range specified in table 1 for isolated photons accompanied by no or at least one hadronic jet. f_{had} denotes the hadronisation correction factor applied to the LO calculation.

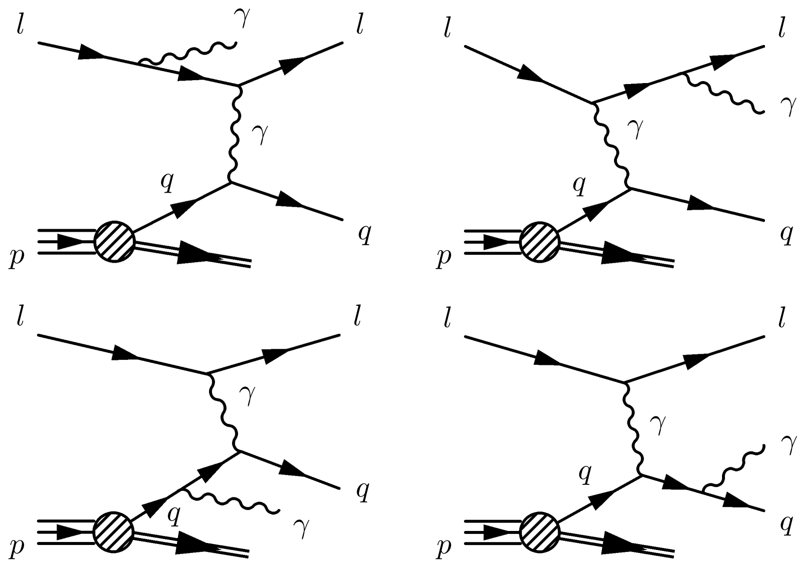

Figure 1: Leading order Feynman graphs for isolated photon production in DIS. The upper diagrams illustrate the isolated photon production by radiation from the electron line (LL), while the lower diagrams correspond to production via radiation from the quark (QQ without the contribution from fragmentation).

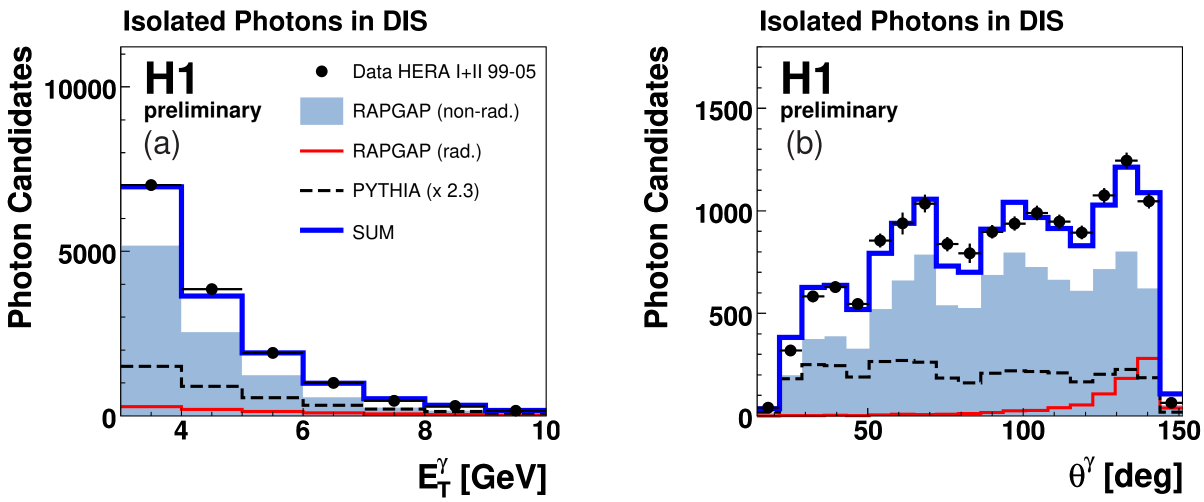

Figure 2: Distributions of (a) E_T^γ and (b) θ^γ for isolated photon candidates that have passed the event selection are shown as points with error bars. The bold solid histogram shows the sum of the expectation from RAPGAP for neutral hadron background (shaded), from PYTHIA for radiation from the quark scaled by a factor of 2.3 (dashed line) and from RAPGAP for radiation from the electron (solid line). The unshaded area corresponds to the expected isolated photon contribution.

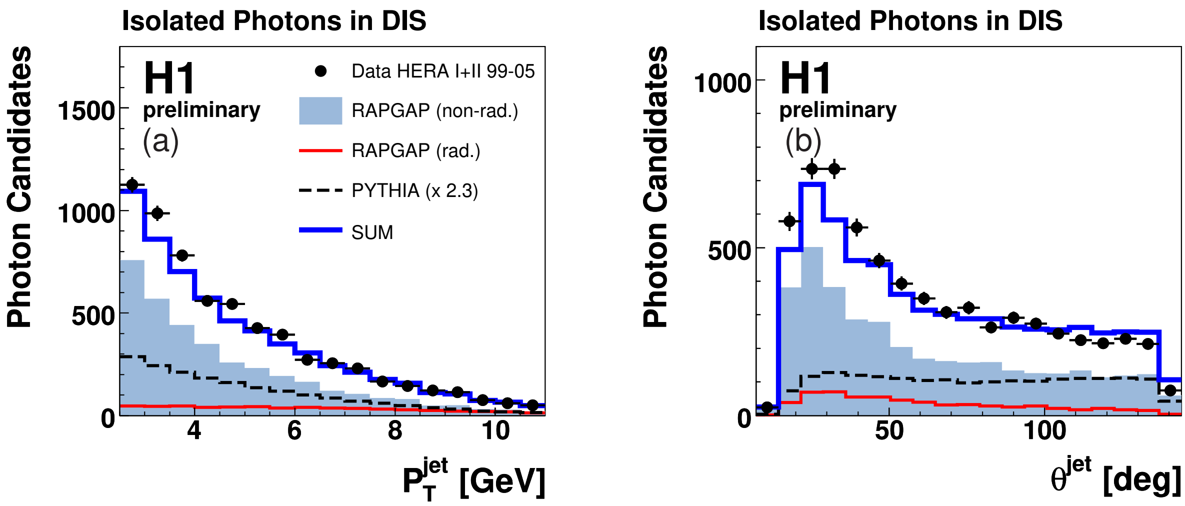

Figure 3: Distributions of (a) the transverse momentum and (b) the polar angle of the hadronic jet with the highest transverse momentum in events with an isolated photon candidate. The data are shown with the MC predictions described in the caption to figure 2.

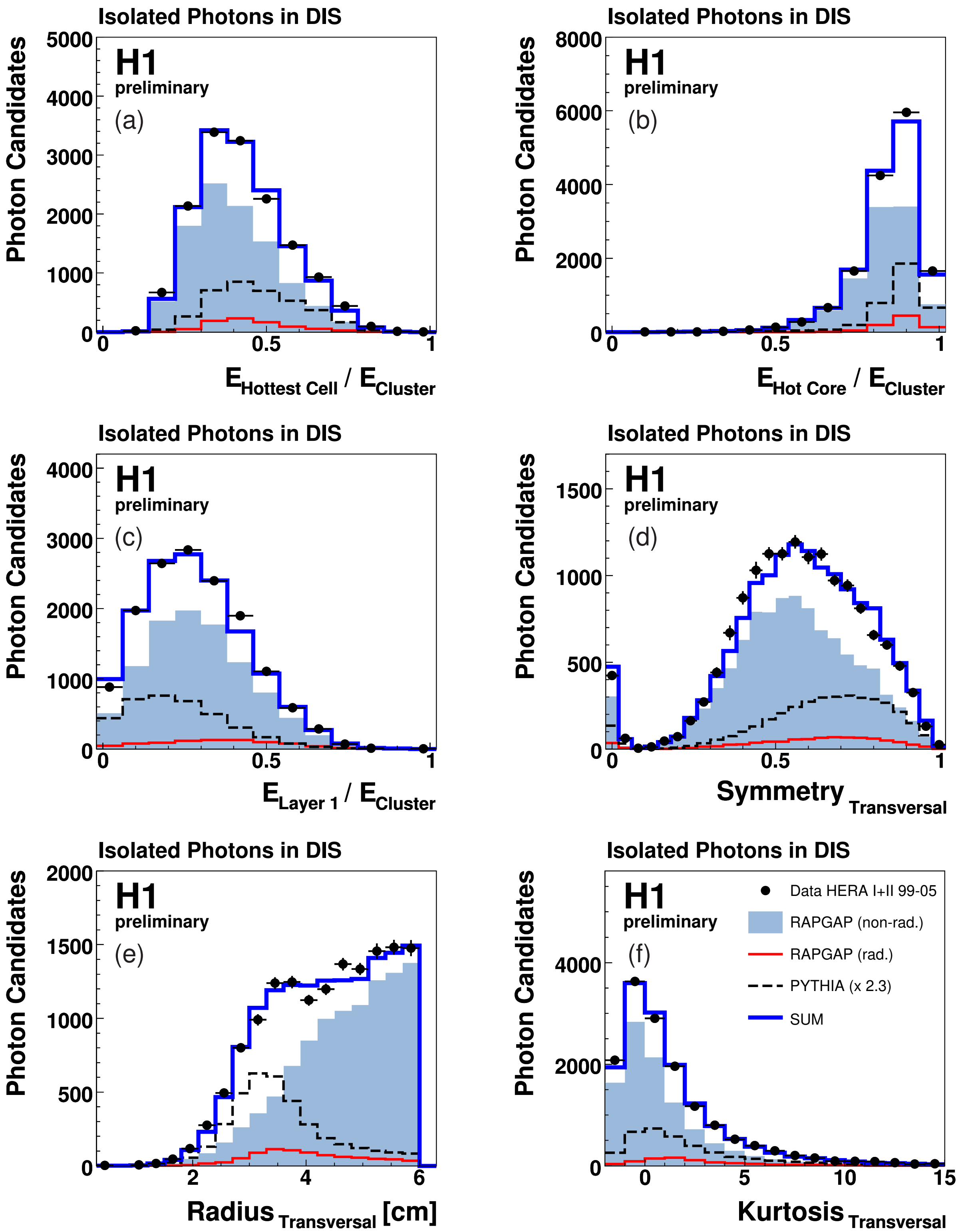

Figure 4: Distributions of the six variables that are used to define the discriminant for isolated photon identification: (a) hottest cell fraction, (b) fraction of the hot core, (c) first layer fraction, (d) transverse symmetry , (e) transverse radius (R_T) and the (f) transverse kurtosis. The data are shown with the MC predictions described in the caption to figure 2. The shape difference between RAPGAP (rad.) and PYTHIA arises from the different distributions in phasespace (see figure 2).

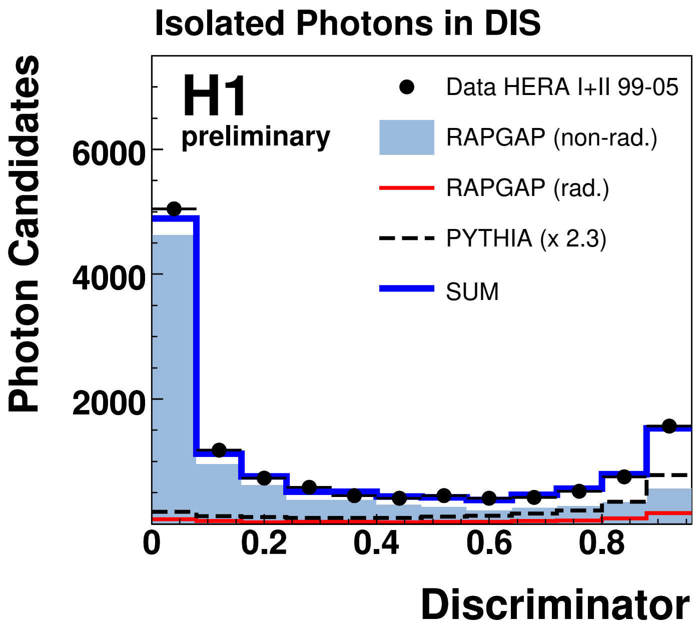

Figure 5: The distribution of the discriminant used in the identification of isolated photon candidates for events that have passed the event selection. The data are shown with the MC predictions described in the caption to figure 2

.

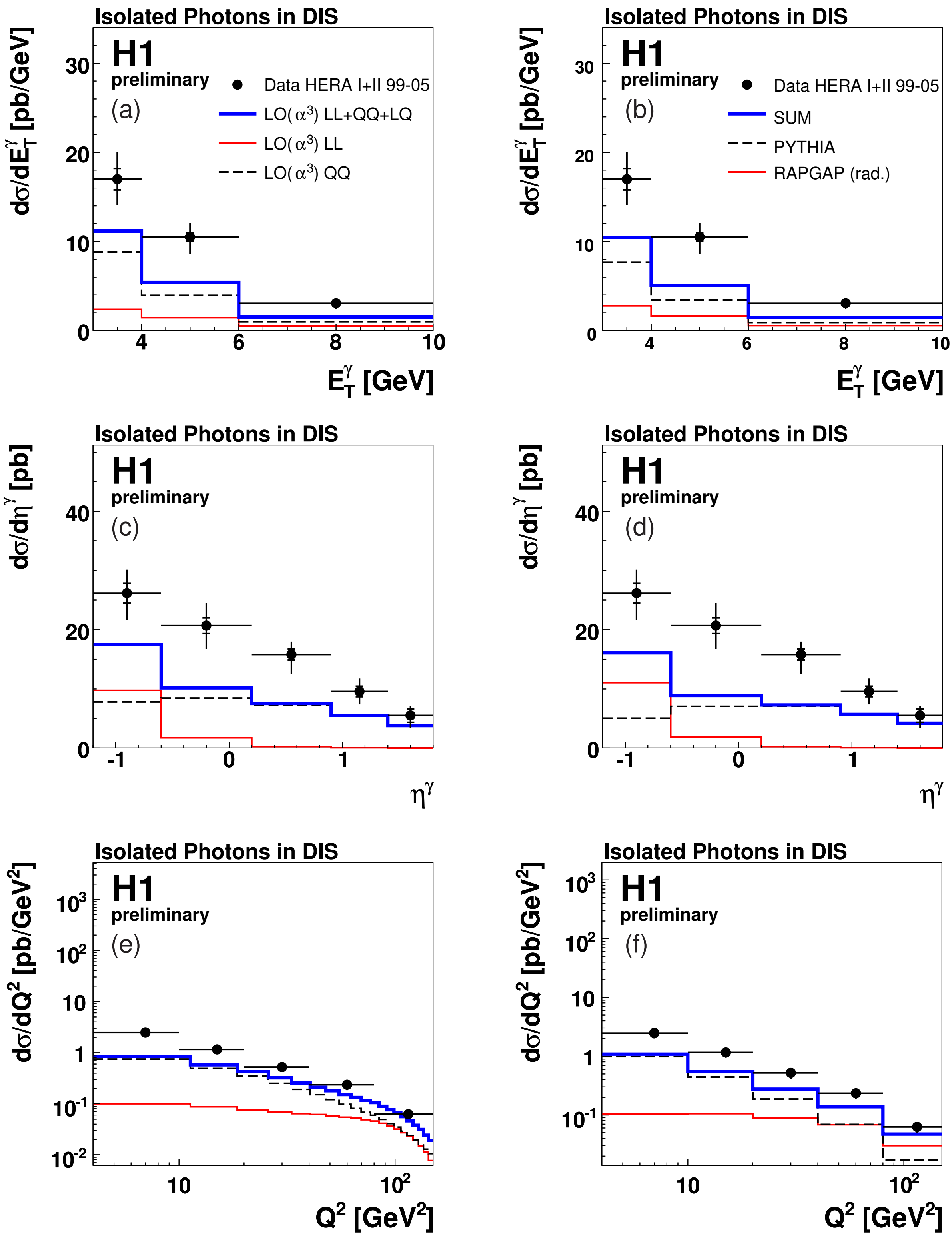

Figure 6: Inclusive differential isolated photon cross sections $d\sigma/dE_T^\gamma$ (a, b), $d\sigma/d\eta^\gamma$ (c, d), and $d\sigma/dQ^2$ (e, f) in the kinematic range specified in table 1. The inner error bars on the data points indicate the statistic error, the full error bars contain in addition the systematical errors added in quadrature. The cross sections in (a), (c) and (e) are shown together with a leading order, $\alpha^3\alpha_s^0$, calculation corrected for hadronisation effects, LL corresponding to radiation from the electron and QQ to radiation from the quark. The same cross sections are shown in (b), (d) and (f) together with the prediction from PYTHIA for photon emission from the quark (dashed line) and from RAPGAP for emission from the electron (solid line).

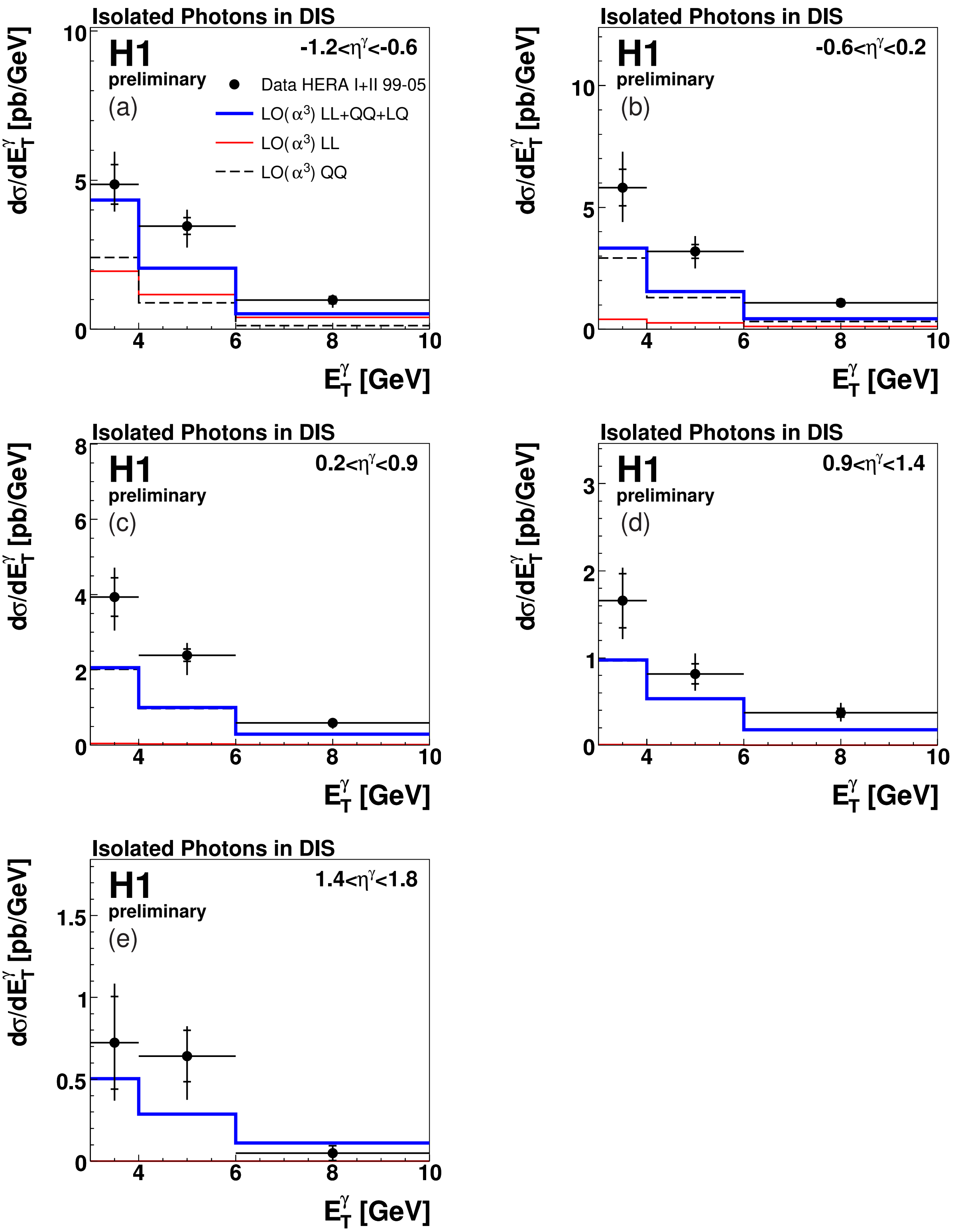

Figure 7: Inclusive differential isolated photon cross sections in the kinematic range specified in table 1 for η^{γ}-bins that correspond to the wheel structure of the LAr calorimeter (see text). The LL contribution is negligible for $\eta^{\gamma} > 0.2$. The measurements are shown with a leading order calculation, as described in the caption to figure 6.

H1 isolated photon production in DIS at $Q^2 > 40$ GeV^2

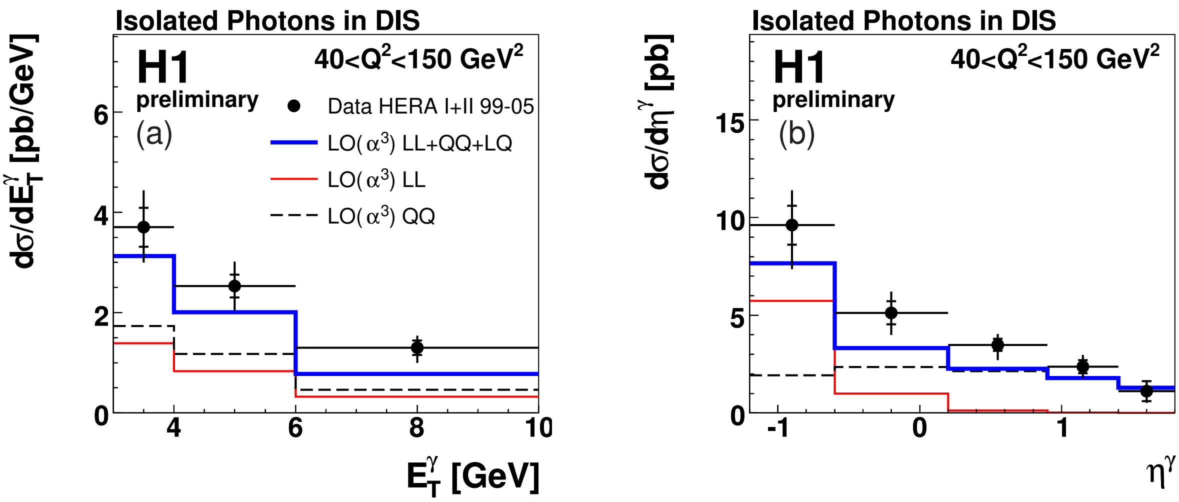

Figure 8: Differential cross sections $d\sigma/dE_T^\gamma$ (a), $d\sigma/d\eta^\gamma$ (b) for the inclusive isolated photon production in the kinematic range specified in table 1 and $40 < Q^2 < 150$ GeV^2. The cross sections are compared to a leading order, $\mathcal{O}(\alpha^3\alpha_s^0)$, calculation as in figure 6.

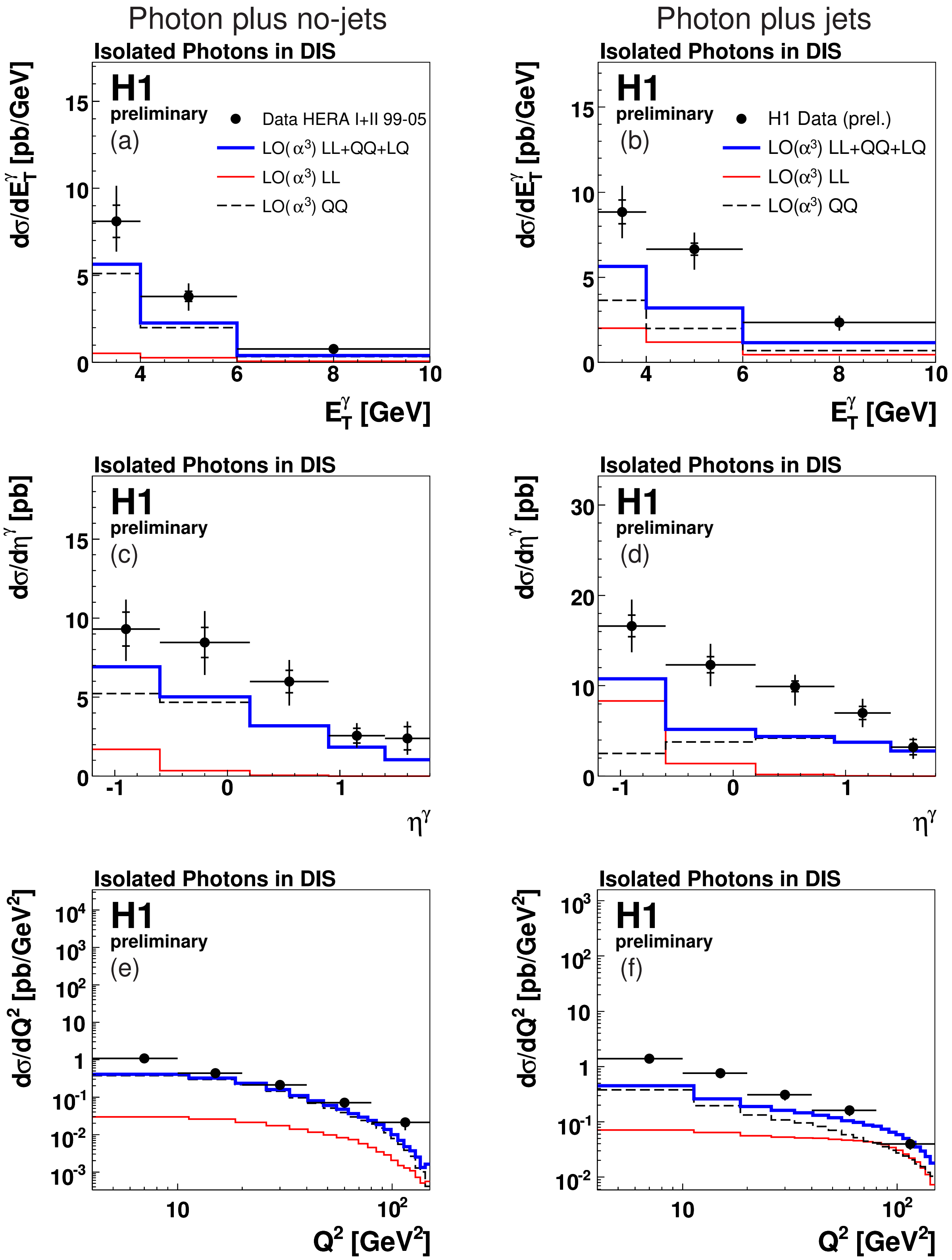

Figure 9: Differential cross sections $d\sigma/dE_T^\gamma$(a, b), $d\sigma/d\eta^\gamma$ (c, d) and $d\sigma/dQ^2$ (e, f) for photon plus no-jets (a, c, e), and photon plus jets (b, d, f) production in the kinematic range specified in table 1. The cross sections are compared to a leading order, $\mathcal{O}(\alpha^3\alpha_s^0)$, calculation as in figure 6.